Space Sci Rev (2007) 131: 105–132
DOI 10.1007/s11214-007-9265-4

The Geophysics of Mercury: Current Status and Anticipated Insights from the MESSENGER Mission

Maria T. Zuber · Oded Aharonson · Jonathan M. Aurnou · Andrew F. Cheng · Steven A. Hauck II · Moritz H. Heimpel · Gregory A. Neumann · Stanton J. Peale · Roger J. Phillips · David E. Smith · Sean C. Solomon · Sabine Stanley

Received: 24 July 2006 / Accepted: 10 August 2007 / Published online: 18 October 2007

M.T. Zuber (✉) · G.A. Neumann · S. Stanley
Department of Earth, Atmospheric and Planetary Sciences, Massachusetts Institute of Technology, Cambridge, MA 02139-4307, USA
e-mail: Zuber@mit.edu

O. Aharonson
Division of Geological and Planetary Sciences, California Institute of Technology, Pasadena, CA 91125, USA

J.M. Aurnou
Department of Earth and Space Sciences, University of California, Los Angeles, CA 90095, USA

A.F. Cheng
The Johns Hopkins University Applied Physics Laboratory, Laurel, MD 20723-6099, USA

S.A. Hauck II
Department of Geological Sciences, Case Western Reserve University, Cleveland, OH 44106, USA

M.H. Heimpel
Department of Physics, University of Alberta, Edmonton, AB, T6G 2J1, Canada

G.A. Neumann · D.E. Smith
Solar System Exploration Division, NASA Goddard Space Flight Center, Greenbelt, MD 20771, USA

S.J. Peale
Department of Physics, University of California, Santa Barbara, CA 93106, USA

R.J. Phillips
Department of Earth and Planetary Sciences, Washington University, St. Louis, MO 63130, USA

S.C. Solomon
Department of Terrestrial Magnetism, Carnegie Institution of Washington, Washington, DC 20015, USA

S. Stanley
Department of Physics, University of Toronto, Toronto, ON, M5S 1A7, Canada

Abstract Current geophysical knowledge of the planet Mercury is based upon observations from ground-based astronomy and flybys of the Mariner 10 spacecraft, along with theoretical and computational studies. Mercury has the highest uncompressed density of the terrestrial planets and by implication has a metallic core with a radius approximately 75% of the planetary radius. Mercury's spin rate is stably locked at 1.5 times the orbital mean motion. Capture into this state is the natural result of tidal evolution if this is the only dissipative process affecting the spin, but the capture probability is enhanced if Mercury's core were molten at the time of capture. The discovery of Mercury's magnetic field by Mariner 10 suggests the possibility that the core is partially molten to the present, a result that is surprising given the planet's size and a surface crater density indicative of early cessation of significant volcanic activity. A present-day liquid outer core within Mercury would require either a core sulfur content of at least several weight percent or an unusual history of heat loss from the planet's core and silicate fraction. A crustal remanent contribution to Mercury's observed magnetic field cannot be ruled out on the basis of current knowledge. Measurements from the MESSENGER orbiter, in combination with continued ground-based observations, hold the promise of setting on a firmer basis our understanding of the structure and evolution of Mercury's interior and the relationship of that evolution to the planet's geological history.

Keywords Mercury · MESSENGER · Core · Rotational state · Magnetic dynamos · Thermal history

1 Introduction

Mercury's internal structure and evolution collectively constitute one of the solar system's most intriguing geophysical enigmas. In terms of its size and surface geology, Mercury is often compared with Earth's Moon. But in striking contrast to the Moon, which is depleted in iron and has a small (if any) metallic core, Mercury's size and mass (Anderson et al. 1987, 1996) indicate a high metal/silica ratio and a metallic mass fraction more than twice that of Earth, Venus, and Mars (Wood et al. 1981). In addition, while the Moon is believed to have cooled rapidly subsequent to accretion (Zuber et al. 1994; Neumann et al. 1996), Mercury appears to possess a liquid outer core (Margot et al. 2007). Such an internal structure is puzzling, as simple thermal evolution models (Cassen et al. 1976; Solomon et al. 1981; Schubert et al. 1988) predict that a pure iron or iron-nickel core should have cooled and solidified by now. A liquid core would survive if there is a sufficient amount of a light alloying element such as sulfur to lower the melting point (Schubert et al. 1988).

Mercury's internal structure and its thermal evolution ultimately must be reconciled with the planet's surface geology. Mercury has a heavily cratered surface (Murray et al. 1974; Murray 1975; Trask and Guest 1975) with ancient compressional tectonic structures that have been taken to imply global contraction (Strom et al. 1975; Watters et al. 1998) associated with secular cooling (Siegfried and Solomon 1974). Ancient intercrater plains and somewhat younger smooth plains of possible volcanic origin (Strom et al. 1975; Trask and Strom 1976; Robinson and Lucey 1997) constrain the early history of the mantle and crustal magmatism.

The evolution of Mercury's core state with time has implications for the planet's spin evolution. Mercury currently displays a 3 : 2 spin–orbit resonance, and the presence of a fluid core would have enhanced considerably its probability of capture into this state (Counselman 1969).

It could be argued that the formation and dynamics of Mercury's core has had a greater influence on the geophysical evolution of the planet than for any other terrestrial planetary

body. Consequently in this paper we treat the core as a point of focus as we review current understanding of Mercury's geophysics. In the context of this review we emphasize recent advances in measuring and interpreting Mercury's rotational state, in interpreting existing magnetic observations, and in convective modeling of the planet's mantle and core. We describe how anticipated future observations from NASA's MErcury Surface, Space ENvironment, Geochemistry, and Ranging (MESSENGER) mission will provide a means of unraveling the unusual characteristics of Mercury's evolution.

2 Physical and Chemical Characteristics

2.1 Geophysical Parameters

The size, shape, and mass of Mercury have been measured from radio tracking of the Mariner 10 spacecraft and Earth-based radar ranging. Current knowledge of these parameters, summarized in Table 1, is based on historical observations as well as more recent reanalysis of combined data sets (Anderson et al. 1987, 1996). Mercury has the largest uncompressed density of the planets (Ringwood 1979) and thus the largest metal/silicate ratio, exhibiting a fractional core mass $M_c/M = 0.65$ (Urey 1951; Siegfried and Solomon 1974), where M is Mercury's total mass. Although the interior has not been sampled, no heavy element other than iron has a cosmic abundance that can account for the observed density. It is believed that the planet has differentiated into an iron-nickel core of radius $R_c/R \sim 0.75$ (Siegfried and Solomon 1974), where R is Mercury's radius. The gravitational flattening (J_2) of Mercury measured by Mariner 10 exceeds the value consistent with hydrostatic equilibrium at Mercury's slow rotation rate. Thus the present J_2 must be either "frozen in" from a more rapid rotation rate in the past (Lambeck and Pullan 1980), or it must be dominated by nonhydrostatic contributions such as the response of a finite-strength lithosphere to the formation and modification of impact basins. Unfortunately the value of J_2 does not in and of itself yield a useful constraint on plausible geochemical models of the radial density distribution of the interior (Solomon 1976).

2.2 Bulk Composition

Beyond inference on fractional iron abundance from the mean density there is no direct information on Mercury's bulk composition (Wood et al. 1981). Solar system condensation models (Lewis 1972) suggest that Mercury is enriched in refractory relative to volatile

Table 1 Shape and bulk properties of Mercury

Parameter	Value
Mass, 10^{23} kg	3.302
Mean radius, km	$2{,}440 \pm 1$
Displacement of center of figure from center of mass in equatorial plane[1], m	640 ± 78
Mean density, kg m^{-3}	5,427
Uncompressed density[2], kg m^{-3}	5,300
Surface gravity, m s^{-2}	3.70
J_2	$(6 \pm 2) \times 10^{-5}$
C_{22}	$(1 \pm 0.5) \times 10^{-5}$

From Yoder (1995) except where noted

[1] Anderson et al. (1996); [2] Wood et al. (1981)

The C_{22} coefficient is unnormalized

elements compared with other terrestrial planets, and an equilibrium condensation scenario (Lewis 1972, 1973) suggests that the silicate fraction of Mercury is dominated by magnesium-rich pyroxene (Wood et al. 1981). Disk-averaged Earth-based visible and infrared spectral observations are consistent with the average composition of anorthositic materials in the lunar highlands (Sprague et al. 1994). The lack of persistent absorption bands identified with mafic minerals limits the average FeO content of surficial materials to less than a few percent (McCord and Clark 1979; Wood et al. 1981; Jeanloz et al. 1995). Explanations for Mercury's high metal content include the differential response of iron and silicate grains to gas drag in the early solar nebula (Weidenschilling 1978), preferential vaporization of silicate relative to metal in the hot solar nebula (Cameron 1985; Fegley and Cameron 1987), and preferential removal of silicate by a giant impact that occurred after Mercury had differentiated (Wetherill 1988). Implications of each of these hypotheses for the chemistry of Mercury's silicate fraction are described at greater length in a companion paper (Boynton et al. 2007).

2.3 Crustal and Mantle Structure

The crustal thickness on Mercury is not presently known. There are no observed surface structural features with regular length scales associated with a subsurface chemical or rheological discontinuity (Zuber 1987) that hint at the existence of a low-density crust (Solomon et al. 1981). Anderson et al. (1996) interpreted the offset between the centers of mass and figure offset for Mercury (Table 1) as indicative of a hemispheric asymmetry in crustal thickness. If interpreted in this context, along with assumptions about internal densities and compositions, the maximum crustal thickness difference between the imaged and unimaged hemispheres of Mercury would be about 13 km. Of course the interpretation of internal structure using the information currently available is highly nonunique, so the use of geophysical and geochemical data sets from MESSENGER will advance considerably the constraints on internal structure.

Barring the existence of diagnostic tectonic structures on the unimaged parts of Mercury's surface, the best chance of estimating crustal and mantle structure may come from future combined analysis of topography (Cavanaugh et al. 2007) and gravity (Srinivasan et al. 2007). Inversions in the spatial and frequency domain will be used to infer crustal thickness and effective elastic lithosphere thickness (cf. Zuber et al. 1994; Simons et al. 1997) on spatial scales comparable with data resolution.

2.4 Orbital and Rotational Parameters

Mercury's modern orbital ephemeris has been developed from radar time-delay and Doppler observations from the Goldstone, Arecibo, and Haystack radio observatories (Harmon et al. 1986; Harmon and Campbell 1988) as well as the three flybys of the Mariner 10 spacecraft (Standish 1990; Standish et al. 1992). These data, combined with radar tracking of the surface, revealed that Mercury exhibits a 3 : 2 spin–orbit resonance (Pettengill and Dyce 1965) that is a consequence of tidal dissipation (Colombo 1965; Colombo and Shapiro 1966; Goldreich and Peale 1966). Orbital information has also been used to refine the perihelion advance of Mercury (Shapiro et al. 1972; Roseveare 1982) predicted by general relativity (Einstein 1916). A summary of Mercury's orbital and rotational parameters is given in Table 2.

Table 2 Orbital and rotational parameters of Mercury

Parameter	Value
Semi-major axis, 10^6 km	57.91
Orbital eccentricity	0.2056
Perihelion, 10^6 km	46.00
Aphelion, 10^6 km	69.82
Sidereal orbital period, Earth days	87.97
Sidereal rotation period, Earth days	58.65
Synodic period with respect to Earth, Earth days	115.88
Mean solar day, Earth days	175.94
Rotation rate $\omega \times 10^5$, s	0.124
Obliquity[1], arc minutes	2.1 ± 0.1

From Yoder (1995) except where noted

[1]Margot et al. (2007)

3 Surface Constraints on Thermal Evolution

The record of impact, volcanism, and tectonism preserved on Mercury's surface places important constraints on models of thermal evolution, and to some extent, on the rotational and orbital evolution. Here we review salient aspects of Mercury's surface geology relevant to the planet's geophysical evolution. Additional details on Mercury's geology can be found in a companion paper (Head et al. 2007).

3.1 Major Impact Basins

The largest impacts experienced by a planet during the late stages of accretion represent a significant source of accretional energy (Safronov 1978; Kaula 1979), establish that crustal formation predated the end of heavy impact bombardment of the solar system, and provide information on the thermomechanical structure of the lithosphere at the time of and subsequent to formation of preserved impact structures. At 1,300 km in diameter, Caloris is the largest well-preserved impact basin on Mercury; other significant basins include Beethoven (625 km in diameter) and Tolstoj (400 km in diameter) (McKinnon 1981). Caloris and Beethoven were only partially imaged by Mariner 10.

Application of models of basin formation and response to loading (Melosh 1978; Melosh and McKinnon 1978; McKinnon and Melosh 1980) constrained by observed deformation has been of limited value in reconstructing Mercury's early thermal state because of the absence of gravity and altimetry, limited imaging coverage of the largest basins, and the paucity of large basins so far identified. The rarity of multiring basins on Mercury in comparison with the Moon may indicate that Mercury's lithosphere was thicker and the planet substantially cooler in comparison with the Moon during late heavy bombardment (Melosh and McKinnon 1988). A rough calculation indicates a lithosphere thickness >100 km for Mercury (McKinnon 1981) in comparison with 25 to >75 km for the Moon (Solomon and Head 1980) for the time of plains loading shortly after the formation of the youngest basins. But such rapid cooling for Mercury is not easily reconciled with preliminary recent evidence for a present-day liquid outer core (Margot et al. 2007). It has also been suggested that early multiring basins were obliterated by viscous relaxation, intercrater plains formation, and subsidence of lithospheric ring blocks (Leake 1982; Melosh and McKinnon 1988). If the paucity of major basins relative to the Moon is ultimately confirmed, other possible explanations, such as the presence of a shallow core–mantle boundary that would limit basin depth and possibly reduce the topographic relaxation time of such structures, should also be investigated.

Shock waves associated with the formation of Caloris may be responsible for disruption of the surface that produced the hilly and lineated terrain at the antipode of the impact (Schultz and Gault 1975b; Hughes et al. 1977; Strom 1984). Early simulations have shown that for a planet-scale event such as Caloris, shock waves can combine constructively at the planet's surface antipodal to the impact (Schultz and Gault 1975a, 1975b; Boslough et al. 1996). The Caloris event could have produced vertical ground movement of about 1 km at the antipode (Hughes et al. 1977), which would require significant acceleration of the surface. Improved modeling may ultimately provide information on the state of Mercury's interior at the time of the largest impacts.

3.2 Volcanism

Mariner 10 images of the surface of Mercury do not show obvious evidence of primary volcanic landforms (Strom et al. 1975; Spudis and Prosser 1984). Some small volcanic structures may have been identified, including domes, rimless pits, crater floor mounds, lineaments, and contrasting crater floor/rim morphology (Dzurisin 1978; Malin 1978; Head et al. 1981) in generally coarse-resolution Mariner 10 images. Ambiguous interpretation of surface structures has been attributed to resolution effects (Head et al. 1981).

Mercury contains two major plains units that have been interpreted by some workers to be a consequence of surface volcanism: older intercrater plains and younger smooth plains (Trask and Strom 1976; Cintala et al. 1977; Strom 1977; Adams et al. 1981; Spudis and Guest 1988). The volcanic origin of the intercrater plains units has been debated, and an alternative interpretation is that these units consist of impact ejecta (Wilhelms 1976; Oberbeck et al. 1977). The intercrater plains correspond to gently rolling terrain between and surrounding areas of heavily cratered terrain and contain craters <10 km in diameter (Trask and Guest 1975). The intercrater plains and heavily cratered terrain have a complex stratigraphic relationship and are not clearly distinguishable in relative age (Trask and Guest 1975; Spudis and Guest 1988). It has been hypothesized that the plains preserve the record of an early resurfacing event (Murray 1975). The intercrater plains are volumetrically significant, obliterating craters smaller than 300–500 km in diameter (Spudis and Guest 1988).

Smooth plains (Strom et al. 1975; Trask and Guest 1975) account for about 15% of Mercury's imaged surface. These units have been viewed as analogous to lunar maria, with the most obvious difference from lunar deposits being the lack of a strong albedo contrast with surrounding cratered terrain (Adams et al. 1981). The smooth plains have albedos comparable to the brightest lunar maria, consistent with that of low-iron, low-titanium basalts (Hapke et al. 1975; Sprague et al. 1994). Combined analysis of opaque mineral abundance, iron content and soil maturity in recalibrated Mariner 10 color mosaics (Robinson and Lucey 1997) has provided the most compelling evidence thus far for a volcanic origin of certain plains units, on the grounds that color boundaries between plains units display lobate geometries consistent with emplacement of surface flows.

3.3 Tectonics

The absence of structural features indicative of plate tectonics argues strongly that Mercury, like the Moon, exhibited a single, continuous mechanical lithosphere from the time of heavy bombardment (Solomon 1978). Mercury's tectonic features are collectively a consequence of secular cooling of the planet, tidal forces, lithospheric loading, and limited local stresses. In further analogy to the Moon, the large Caloris basin contains what appear to be contractional (thrust) and extensional (graben) structures that are likely a consequence of basin

loading and viscoelastic relaxation (Maxwell and Gifford 1980; Fleitout and Thomas 1982; Melosh and McKinnon 1988; Thomas et al. 1988). If smooth plains are volcanic in origin, fractures in the basin floor may represent the surface expression of conduits that enabled the upward transport of magma (Burke et al. 1981).

Unlike the Moon, the part of Mercury's surface imaged by Mariner 10 shows evidence for a regional to global distribution of tectonic landforms that include ridges, troughs, and lineaments of ambiguous origin (Dzurisin 1978; Burke et al. 1981; Melosh and McKinnon 1988). The most prominently expressed features are lobate scarps (Strom et al. 1975), which have been interpreted as the surface expressions of large-offset thrust faults (Strom et al. 1975; Dzurisin 1978; Strom 1979). The scarps are arcuate to quasi-linear, 20–500 km-long structures that crosscut various terrains. Early work suggested a more or less uniform distribution over the imaged part of Mercury's surface (Strom et al. 1975), which favored an origin due to global contraction. More recent mapping (Watters et al. 2004) shows that there is a higher density of scarps in the imaged hemisphere of Mercury at latitudes poleward of 50°S, which suggests that regional stresses also played a role. The observation that some scarps are disrupted by large craters has been interpreted to indicate that scarp formation was ongoing during the later stages of heavy bombardment (Burke et al. 1981), but the presence of scarps on the smooth plains indicates that thrust faulting continued after smooth plains emplacement (Strom 1979). The shortening associated with lobate scarps in the imaged hemisphere of Mercury implies horizontal surface strains of $\sim 0.05-0.1\%$, corresponding to a $\sim 1-2$ km decrease in the planet's radius (Strom et al. 1975; Watters et al. 1998). Global contraction of this magnitude is also predicted by some thermal history models (Solomon 1976, 1977).

Mercury's lobate scarps have alternatively been interpreted as a consequence of despinning by solar tides (Burns 1976; Melosh and Dzurisin 1978) that also led to Mercury's current spin–orbit resonance (Goldreich and Peale 1966; Colombo and Shapiro 1966). Although predicted low-latitude scarps are observed, the expected high-latitude extensional features (Melosh 1977) have not yet been observed. The known distribution of tectonic features dictates that global contraction is required to explain the deformation whether or not despinning contributed to the lithospheric stress field.

4 Information from the Rotational State

4.1 Spin–Orbit Resonance

Mercury is unique among all solar system bodies in that its rotational angular velocity is stabilized at 1.5 times its orbital mean motion. Figure 1 shows schematically this commensurate spin. Here the stability against the secular tidal slowing of the spin is effected by the average torque on the permanent asymmetry, which tends to keep the axis of minimum moment of inertia aligned toward the Sun as Mercury passes through perihelion (Colombo 1965; Goldreich and Peale 1966). Tidal friction naturally slows an initially higher spin, and Mercury would have had opportunity to be captured into any of several stable resonant spin states with angular velocities that are half-integer multiples of the mean motion, n. The probability of capture into one of the spin–orbit resonances, as the spin rate is slowed by tides, increases as the order of the resonance decreases. The $3:2$ resonance has the highest probability of capture of any of those previously encountered if tides were the only dissipative force acting and if the current orbital eccentricity prevailed (Goldreich and Peale 1966). The chaotic nature of the orbital motion in the solar system leads to much wider excursions in Mercury's orbital eccentricity ($\sim 0-0.325$) than were obtained in the previously

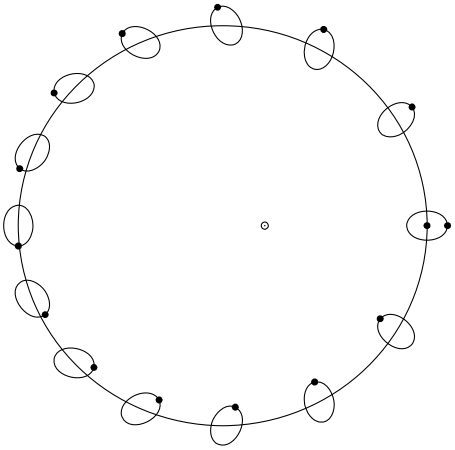

Fig. 1 Rotation of Mercury in the 3 : 2 spin–orbit resonance. The *dot on the orbital curve* marks the perihelion of the orbit, whereas the *dots on the small ellipses* representing Mercury mark one end of the axis of minimum moment of inertia. The Mercury ellipses are separated by equal time intervals

assumed quasi-periodic motion (0.11–0.24). Repeated passes of Mercury's spin through the spin–orbit resonances in both directions thereby yield capture into the 3 : 2 resonance after 4.5×10^9 yr in 55% of trial evolutionary simulations (Correia and Laskar 2004).

The probability for capture into the spin–orbit resonances increases substantially if Mercury's mantle were decoupled from the core by a liquid layer during the time of resonance passage (Counselman and Shapiro 1970). There is thereby a relatively large probability of capture into the 2 : 1 spin resonance that is a function of the core viscosity, the tidal dissipation function, the orbital eccentricity at the time of passage, and the value of $(B - A)/C_m$, where $A < B < C$ are the principal moments of inertia of Mercury and C_m is the moment of inertia of the mantle and crust about the spin axis. For a kinematic core viscosity of 10^{-6} $m^2\ s^{-1}$ and plausible choices for the other parameters, the probability of capture can exceed 0.5 (Peale and Boss 1977). However, even if capture into the 2 : 1 resonance were to have occurred, the chaotic evolution of Mercury's orbit can lead to escape from this resonance as the eccentricity falls below a critical value near 0.005, where the resonance becomes unstable (Correia and Laskar 2004).

4.2 Determination of Core State

A procedure for ascertaining the nature of Mercury's core from precise determination of the rotation state (Peale 1976; Peale et al. 2002) depends on

$$\left(\frac{C_m}{B-A}\right)\left(\frac{B-A}{MR^2}\right)\left(\frac{MR^2}{C}\right) = \frac{C_m}{C} \le 1. \tag{1}$$

The following equations determine the factors in (1):

$$\begin{aligned} \phi_0 &= \frac{3}{2}\frac{B-A}{C_m}\left(1 - 11e^2 + \frac{959}{48}e^4 + \cdots\right), \\ \frac{C}{MR^2} &= \frac{[\frac{J_2}{(1-e^2)^{3/2}} + 2C_{22}(\frac{7}{2}e - \frac{123}{16}e^3)]\frac{n}{\mu}}{(\sin I)/i_c - \cos I}, \\ \frac{B-A}{MR^2} &= 4C_{22}. \end{aligned} \tag{2}$$

In (2), ϕ_o is the amplitude of the physical libration, which is the maximum deviation of the axis of minimum moment of inertia from the position it would have had if the rotation were uniform at $1.5n$, i_c is the obliquity of the Cassini state, the state that Mercury's spin axis is expected to occupy, J_2 and C_{22} are the second degree zonal and tesseral spherical harmonic coefficients, respectively, in the harmonic expansion of Mercury's gravitational field, e is the orbital eccentricity, and I is the inclination of the orbit plane to the Laplacian plane on which the orbit precesses at the uniform rate $-\mu$. [See Peale (1969, 1974) for a discussion of generalized Cassini's laws.] From virtually any initial obliquity, tidal and core–mantle dissipation drive Mercury's spin to the Cassini state (Peale 1974; Ward 1975), in which state the spin axis and orbit normal remain coplanar with the normal to the Laplace plane as both of the former precess around the latter with the ∼300,000-year period of the orbital precession. The spin axis is fixed in and precesses with the orbit frame of reference if Mercury is in the Cassini state. Otherwise, it precesses around this state with a 500- or 1,000-year period, depending on whether the core follows the mantle precession (Peale 2005).

The forced physical libration, with a period of 88 days, is due to the reversing torque on Mercury as it rotates relative to the Mercury–Sun line, as shown in Fig. 1. The amplitude of this libration is inversely proportional to the moment of inertia C_m of the mantle and crust in the first part of (2) because the liquid core does not follow the short-period librations of the mantle. In addition, the full polar moment of inertia C appears in the second part of (2) because the core is likely to follow the mantle during its 300,000-year precession with the orbit (see Sect. 4.3). These two conditions are necessary for the success of the experiment in determining C_m/C, which will be near a value of 0.5 in most models of Mercury's interior (Siegfried and Solomon 1974). If C_m/C in (1) were equal to 1, it would mean that C_m would be replaced by C in the first factor in (1), and the core would be firmly coupled for the long and short timescales. The conditions for determining core state are satisfied for a wide range of core viscosities that include all current estimates of the viscosity of the Earth's core (Peale 1976, 1981, 1988; Peale et al. 2002).

The only unknowns in (2) are ϕ_o, i_c, J_2, and C_{22}. In the MESSENGER mission (Solomon et al. 2001), all of the required parameters will be estimated or improved via the altimetry (Cavanaugh et al. 2007) and radio science (Srinivasan et al. 2007) experiments, and the first two are also measurable by Earth-based radar (Holin 1988, 1992, 2003; Margot et al. 2007). In addition, measurement of the forced libration will be accomplished as part of the MESSENGER mission by estimating independently the libration of the surface from altimetry and the interior from gravity using long-wavelength shapes of the global fields (Zuber and Smith 1997). Table 3 summarizes the expected recovery of geophysical parameters using a simulation of the approximate MESSENGER mission scenario (Zuber and Smith 1997). Because of MESSENGER's elliptical orbit, coverage of the surface from the Mercury Laser Altimeter (MLA) (Cavanaugh et al. 2007) will be limited to the northern hemisphere; radio occultations of the spacecraft will be used to constrain planetary shape in the southern hemisphere (Srinivasan et al. 2007). The latitude-dependent resolution of the gravity field will permit study of crustal and lithospheric structure for much of the northern hemisphere where information at spherical harmonic degrees as high as 76 (spatial resolution 100 km) will be resolvable, while in the southern hemisphere only the lowest degree harmonics (no higher than 10; relevant for deep internal structure and libration recovery) will be obtained. Because of the nonuniform resolution expected, spherical harmonics are not optimum and other representations of the gravity field will be investigated.

Table 3 Simulated geophysical parameter recovery from MESSENGER

Parameter	A priori value	Recovery from gravity	Recovery from altimetry
Libration amplitude in longitude, radians	1.435×10^{-4}	1.542×10^{-4}	1.568×10^{-4}
Libration amplitude in longitude, m	350	376, 7% error	386, 9% error
Obliquity, arcsec	0.0	2.0	0.2
Gravity			
C_{20}	-2.7×10^{-5}	-2.688×10^{-5} (0.5% error)	–
C_{22}	1.6×10^{-5}	1.598×10^{-5} (0.2% error)	–
S_{22}	0.0	1.4×10^{-5}	–
Topography			
C_{20}, m	−733	–	−754 (3% error)
C_{22}, m	72	–	180 m (150% error)
S_{22}, m	395	–	447 m (13% error)

C_{lm} and S_{lm} are spherical harmonic coefficients, where l and m represent degree and order of the spherical harmonic expansion. All coefficients are normalized according to Kaula (1966). Note that $C_{20} = -J_2/(5)^{1/2}$. Simulation described by Zuber and Smith (1997)

4.3 Core–Mantle Coupling

Previous work (Peale 1976, 1981) has indicated that viscous coupling of a liquid core and mantle satisfies the criterion that the core not follow the mantle on the 88-day timescale of the physical libration but does follow the mantle on the 300,000-year timescale of the precession for a wide range of plausible viscosities. More recent work (Peale et al. 2002) shows that core–mantle coupling due to magnetic fields (Buffett 1992; Buffett et al. 2000), to topography on the core–mantle boundary (CMB) (Hide 1989), and to gravitational interaction between the mantle and an asymmetric inner core (Szeto and Xu 1997), are not likely to frustrate the condition that the liquid core not follow the mantle on the 88-day libration timescale.

Inertial (pressure) coupling of the core to the mantle could compromise the experiment by affecting either the libration in longitude or the spin precession. It is likely that any deviations of the circularity of the CMB equator will be no larger than possible topography induced by convection cells in the mantle whose horizontal extent is not significantly larger than the mantle thickness (Hide 1989). It is therefore necessary to consider only a possible effect of the pressure coupling on the precession of the spin axis. The criterion that pressure at an elliptical CMB couples the core to the mantle is (Stewartson and Roberts 1963; Toomre 1966)

$$\dot{\Omega}/\dot{\psi} < \varepsilon, \tag{3}$$

where $\dot{\psi}$ is the rotational angular velocity, $\dot{\Omega}$ is the precessional angular velocity $\varepsilon = (a - c)/a$ is the core ellipticity, and a and c are the equatorial and polar radii of the CMB, respectively. If we assume for the moment that the entire planet is in hydrostatic equilibrium,

then

$$J_2 = \frac{k_f R^3 \dot{\psi}^2}{3GM}, \tag{4}$$

where k_f is the fluid Love number (Munk and MacDonald 1960), and G is the gravitational constant. We also note that, to lowest order (Kaula 1968),

$$J_2 \approx \frac{2}{3}\varepsilon - \frac{\dot{\psi} R^3}{3GM}. \tag{5}$$

The ε in (5) refers to the entire planet. The ellipticity of the CMB will depend on the radial density distribution, but since the core radius is $\sim 0.75R$, the ellipticity of the CMB will not be much smaller than this ε if hydrostatic equilibrium prevails as assumed here. The two expressions for J_2 may be combined to yield

$$\varepsilon = 4.5 \times 10^{-7} \frac{1 + k_f}{2} \frac{\dot{\psi}^2}{n^2}, \tag{6}$$

so pressure coupling would occur if

$$\frac{\dot{\Omega}}{\dot{\psi}} = 3.2 \times 10^{-4} \leq 4.5 \times 10^{-7} \frac{\dot{\psi}^2}{n^2}, \tag{7}$$

which is true if $\dot{\psi}/n > 26.7$. This ratio is so large that it allows some relaxation from the assumption of strict isostasy. Since $\dot{\psi}/n = 1.5$, pressure coupling of the core to the mantle is completely negligible.

4.4 Free Motions?

There are possible situations where Mercury would not occupy the precise equilibrium state as described that constrains the core properties. A large impact or other unspecified excitation mechanism could excite the three free rotational motions. These include a free libration in longitude, a free precession of the spin vector about the Cassini state, and a free wobble, where "free" means that the amplitudes and phases of these motions are arbitrary. The free libration in longitude results if Mercury's axis of minimum moment of inertia is displaced from the Mercury–Sun line when Mercury is at perihelion (Fig. 1). The gravitational torque on the asymmetric planet, averaged around the orbit, acts to restore this alignment so that the long axis will tend to librate around the solar direction at perihelion. The period of this libration is close to 12 y. The short-period torque reversals causing the 88-day physical libration average to zero in this application. A free precession is characterized by a displacement of the spin axis from the Cassini state position; this displacement leads to a precession of the spin axis about the Cassini state with an approximately constant angular separation. The period of this precession is about 500 y if the liquid core is not dragged along with the mantle, and double that time if it is. A free wobble is the precession of the spin vector around the axis of maximum moment of inertia in the body frame of reference. It is also called nonprincipal axis rotation. The period of spin vector excursion in the body frame of reference is about 300 years if only the mantle and crust participate. Because the duration of measurements by MESSENGER is much shorter than this period, and the proposed measurements will be unable to detect a free wobble, we consider it no further here.

Free motions are subject to dissipative damping, both from tides and from the relative motion of the liquid core and solid mantle. Whether we should expect to find free motions depends on the timescales for damping of such motions, which are given by (Peale 2005)

$$T_{\rm lib} = \frac{2.92 \text{ years}}{1.41 \times 10^{-4} \nu^{1/2} + 3.93 \times 10^{-4} \frac{k_2}{Q_0}} = 1.8 \times 10^5 \text{ years},$$
$$T_{\rm prec} = \frac{89 \text{ years}}{8.59 \times 10^{-3} \nu^{1/2} + 8.08 \times 10^{-3} \frac{k_2}{Q_0}} = 1.0 \times 10^5 \text{ years}, \quad (8)$$

where $T_{\rm lib}$ and $T_{\rm prec}$ are the damping timescales for the free libration and the amplitude of the free precession, respectively. In (8), ν is the kinematic viscosity in cm^2/s, k_2 is the second-degree tidal Love number (Munk and MacDonald 1960), and Q_o is the tidal dissipation function at a tidal period corresponding to the orbit period. The tidal model is equivalent to the assumption that Q is inversely proportional to frequency. The torque between the liquid core and solid mantle is assumed to be proportional to the difference between the vector angular velocities of the core and mantle. The proportionality constant is related to the kinematic viscosity of the core fluid by equating the timescale for the damping of a differential velocity between core and mantle to the timescale for the relaxation of the differential motion of a fluid inside a rotating, closed container of radius $R_c [T = R_c/(\dot{\psi}\nu)^{1/2}]$ (Greenspan and Howard 1963). [Further details in calculating the timescales in (8) were given by Peale (2005).] The analytical expressions for the timescales shown in (8) are verified by numerical integration of the complete equations of motion for $\nu = 0.01$ $\text{cm}^2\,\text{s}^{-1}$ and $k_2/Q_o = 0.004$, values that yield the numerical estimates on the right-hand sides of these equations. The value of ν is in the middle of a rather small range estimated for the Earth's core (de Wijs et al. 1998), and the value of k_2/Q_o is comparable to that appropriate to Mars (Smith and Born 1976; Yoder et al. 2003; Bills et al. 2005).

The timescales for damping the free libration in longitude and the free precession are both short compared with the age of the solar system, so ordinarily we would expect both to be damped to undetectable magnitudes. However, the small variations in the orbital elements due to the planetary perturbations induce long periods of forced librations dominated by a 5.93-year variation, which is half of Jupiter's orbital period (Peale et al. 2007). There will also be a small amplitude variation near the free libration period of about 12 years due to a near resonance of the orbital variations at Jupiter's orbital period. This latter variation may have been seen in the recent radar data (Margot et al. 2007).

Because the forced physical libration period is much shorter than that of the free libration, any measurable amplitude of the latter will not compromise the determination of the former's amplitude. The physical libration will simply be superposed on the longer-period free libration as shown in Fig. 2. However, a significant amplitude of the free precession would mean that the spin axis would not be coincident with the Cassini state, and the thereby uncertain position for the latter would make the determination of C/MR^2 via the second equation in (2) more uncertain. If Mercury's spin is in the Cassini state, it is coplanar with the orbit normal and the Laplace plane normal. The straight line in Fig. 3 represents the intersection of the plane defined by the orbit normal and the Laplace plane normal with the unit sphere centered on the coordinate system origin. Then the spin axis would intersect the unit sphere at a point on this line. If there is a finite-amplitude free precession, the spin axis would be offset from this position on a circular precession trajectory at some arbitrary phase. Figure 3 shows an example position determined observationally that would be indicative of a free precession along with a segment of its precession trajectory.

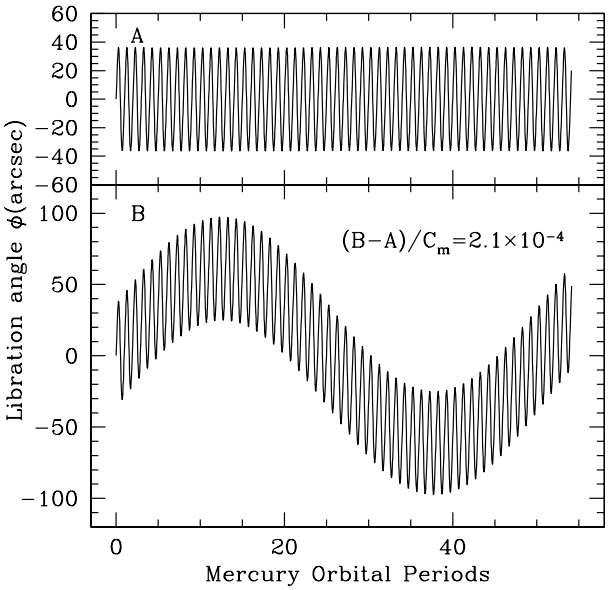

Fig. 2 **(A)** Physical libration of Mercury with no free libration. **(B)** Physical libration of Mercury superposed on a small free libration. The free libration does not hinder measurement of the physical libration amplitude

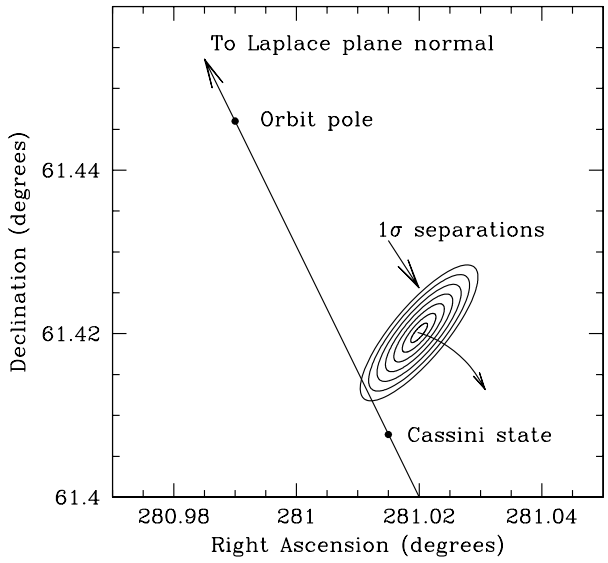

Fig. 3 Signature of a free precession showing the offset of the spin position from the Cassini state. The *straight line* is the intersection of the plane defined by the orbit normal and the Laplace plane normal with the unit sphere. The Cassini state is coplanar with the orbit normal and the Laplace plane normal, and a unit vector in the Cassini state direction intersects the unit sphere on this line as shown. The uncertainty contours surround the least squares fit to the hypothetical observed position of the spin axis. The *curved arrow* is a portion of the spin precession trajectory on the unit sphere

4.5 The Changing Cassini State Position

There is another possible deviation of the spin axis from the Cassini state in addition to a free precession. The second equation in (2) shows the dependence of the Cassini state on the orbital parameters, which includes the orientation of the Laplace plane. The variation in the orbital parameters due to planetary perturbations, and the similarly slow change in the geometry of the planets, means that the position of the Laplace plane and of the Cassini state will change on the same timescales. However, an action integral, which is proportional

to the solid angle swept out by the spin vector as it precesses around the Cassini state, is an adiabatic invariant if the precession is fast relative to the slow changes in the parameters that define the Cassini state (Goldreich and Toomre 1969; Peale 1974). As the timescales for the slow variations usually exceed 10^5 y and the precession period is 500 or 1,000 y, one expects the adiabatic invariant to keep the spin close to the instantaneous value of the Cassini state as the latter's position slowly changes. The adiabatic invariant is not conserved for the short-period fluctuations in the orbital elements. However, these short-period fluctuations are of small amplitude, and one expects the deviations of the spin vector from the Cassini state to be commensurate with these amplitudes. The increasing precision of the radar determinations of Mercury's spin properties, and that anticipated for the MESSENGER mission, warrant a check on just how closely the spin axis follows the changing position of the Cassini state.

By following simultaneously the spin position and the Cassini state position during long-timescale orbital variations over the past 3 My (Quinn et al. 1991) and short-timescale variations for 20,000 y (Jet Propulsion Laboratory Ephemeris DE 408, E.M. Standish, private communication 2005), Peale (2006) showed that the spin axis remains within one arcsec of the Cassini state after it is brought there by dissipative torques. In Fig. 4 the variations of Mercury's eccentricity and inclination to the ecliptic of year 2000 are shown for the last 3×10^6 y from data obtained from a simulation by T. Quinn (ftp://ftp.astro.washington.edu/pub/hpcc/QTD). On this same timescale, the ascending node of the orbit plane on the ecliptic generally regresses, with fluctuations in the rate. The Quinn data have been filtered to eliminate periods less than 2,000 y. It is therefore necessary to check also the effect of short-period variations. Figure 5 shows the variation of e, I, and Ω over the 20,000-y time span of the JPL DE 408 ephemeris, where Ω is the longitude of the ascending node of the orbit plane on the ecliptic. Short-period fluctuations are superposed on the almost linear trend of these variables, where the amplitudes are comparable to the line widths. Generally, the parameters e, I, Ω, dI/dt, and $d\Omega/dt$ affect the Cassini state position. The angular velocity of the orbit plane can be represented by the vector sum of dI/dt and $d\Omega/dt$ averaged over a suitable interval, say 2,000 y. This angular velocity, while suitable for use in the equations of motion, is not the instantaneous value of μ in the second equation of (2), since another con-

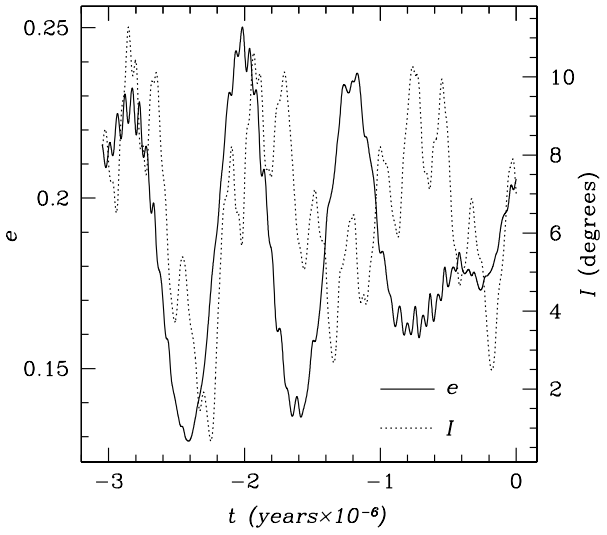

Fig. 4 Variation of Mercury's eccentricity, e (*solid line*), and orbital inclination, I (*dotted line*), to the ecliptic of year 2000, from T. Quinn (ftp://ftp.astro.washington.edu/pub/hpcc/QTD)

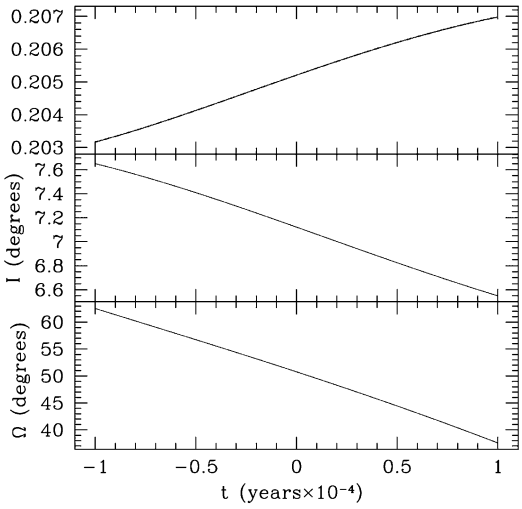

Fig. 5 Variation of e, I, and Ω relative to the ecliptic of J2000 for JPL Ephemeris DE 408. From Peale (2005)

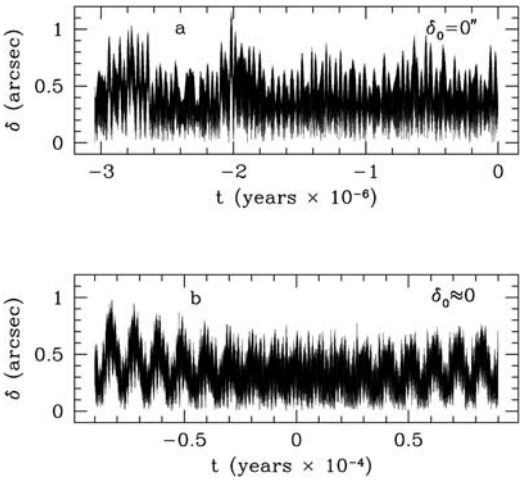

Fig. 6 Angular separation of Mercury's spin axis from Cassini state 1: **(a)** For long-timescale variations over 3×10^6 y from simulations by T. Quinn. **(b)** For short-time-scale variations over 20,000 y from JPL Ephemeris DE 408 provided by E.M. Standish. The periodic variation in δ results from the spin precession around the Cassini state

straint is necessary to determine the Laplace plane orientation (Yseboodt and Margot 2006; Peale 2006).

The equations of variation of the spin position in the orbit frame of reference are numerically integrated with the five parameters e, I, Ω, dI/dt, and $d\Omega/dt$ determined at arbitrary times from spline fits to the data. The position of the Cassini state is followed simultaneously, and the proximity of the spin to the Cassini state is determined as a function of time. Since dissipation will drive the spin to the Cassini state, we start the spin in this state initially and allow the evolution to proceed. The angle δ between the spin and Cassini state positions is shown in Fig. 6 for both the long- and short-timescale variations in the orbital parameters. The fluctuations in δ are generally $<1''$ as asserted earlier. If the spin is started somewhat displaced from the Cassini state, the initial displacement is maintained to within $1''$ as the spin precesses around the Cassini state, which is consistent with the adiabatic invariance of the solid angle described by the spin. Aside from superposed, small-amplitude fluctuations,

an initial displacement for the short-period orbital variations is also maintained to the same precision.

It is apparent that the real orbital element variations will not cause the spin to deviate from the Cassini state by more than 1″, even with no damping. This conclusion leaves an unlikely free precession as the only reason the spin vector might be displaced from the Cassini state by a measurable amount unless tidal and core–mantle dissipation displaces the spin significantly such as that which occurs for the Moon (Williams et al. 2001). The experiment to determine the nature and extent of Mercury's core from the details of the rotation is thus likely to be successful.

5 Magnetic Field: Observations and Possible Explanations

5.1 Observations from Mariner 10

Two of the three flybys of Mercury by the Mariner 10 spacecraft resulted in the surprising measurement of a planetary magnetic field and magnetosphere (Ness et al. 1974, 1975, 1976). Mercury's magnetosphere, reviewed in a companion paper (Slavin et al. 2007), exhibits a bow shock and a magnetopause, which are manifest as well-resolved discontinuities in the Mariner 10 magnetometer and plasma observations (Russell et al. 1988). The magnetic field is characterized by a dominantly dipolar structure with the same polarity as Earth's present field. Mercury's field is aligned approximately with the ecliptic normal and has a moment of 300 nT-R_M^3 (Connerney and Ness 1988). Because of its intensity, the observed field cannot be a consequence of solar wind induction (Herbert et al. 1976) and is likely of internal origin (Ness et al. 1975, 1976). Two possible interpretations of an internal field include remanent magnetization of Mercury's crust and a present-day dynamo generated in a liquid iron core.

5.2 Remanent Magnetization

Thermoremanent magnetization acquired by igneous rocks that cooled below the Curie temperature of mineral magnetic carriers during the presence of an ambient field has been documented on Earth, the Moon, and Mars and can be expected for at least some areas of the crust of Mercury. Remanence has the appealing feature that it could explain the Mariner 10 observations in the event that Mercury's core has either solidified or is partially liquid but is not sufficiently well-stirred by convection to generate dynamo action (Stevenson 1983; Stevenson et al. 1983). A crustal source for Mercury's field was originally dismissed (Ness 1978, 1979; Connerney and Ness 1988), but new planetary magnetic observations combined with experiment and theory have collectively caused the possibility to be revisited (Aharonson et al. 2004).

First, large coherent structures with sufficiently high remanent magnetization to explain the Mariner 10 observations were not believed to exist in the terrestrial planets. However, the Mars Global Surveyor mission has since provided magnetic observations of Mars pointing to a crustal field of high specific magnetization ($\sim$20 A m^{-1}) (Acuña et al. 1998, 1999, 2001) with horizontal scales for coherence of magnetization direction of hundreds of kilometers. In addition, laboratory experiments have shown that single- and multidomain thermoremanent magnetization in some iron oxide-rich minerals can be significant (Kletetschka et al. 2000a, 2000b). Although highly oxidized minerals (hematite, magnetite) may not be present in the FeO-poor, water-poor crust of Mercury, other magnetic minerals such as pyrrhotite are more likely to be present and can potentially carry magnetic remanence (Rochette et al. 2001).

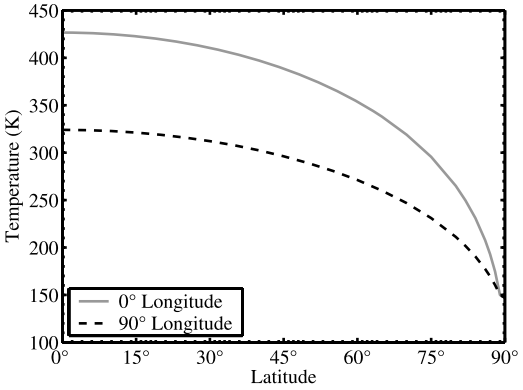

Fig. 7 Spherical harmonic fits to Mercury's near-surface temperature (diurnal variations averaged out) from the model of Aharonson et al. (2004). Strong latitudinal and longitudinal dependence is predicted and seen. A spherical planet has been assumed

Another reason for excluding remanence derived from a simple theorem in magnetostatics (Runcorn 1975a, 1975b): a uniform shell magnetized by an internal source subsequently removed has no external field. This theorem, known as Runcorn's theorem, dictates that even if magnetic minerals were present in Mercury's crust, they could not produce an external remanent field if they were distributed uniformly (Srnka 1976; Stephenson 1976). However, it has recently been shown (Aharonson et al. 2004) that latitudinally and longitudinally varying solar insolation could lead to long-wavelength variations in the depth to the Curie temperature, and thus the spatial distribution and intensity of remanent magnetization. As is apparent from Fig. 1, Mercury's 3 : 2 spin orbit resonance causes the planet to have two equatorial "hot poles," at 0° and 180° longitude. In addition, Mercury's surface temperature also varies latitudinally, with the greatest insolation at low latitudes. Figure 7 shows the expected latitudinal pattern of surface temperature on Mercury at two longitudes. Because of solar insolation and Mercury's rotational and orbital orientations, therefore, surface temperature is a maximum at the equator and decreases toward the north and south poles.

Such a crustal thermal structure breaks the previously assumed symmetry of Mercury's magnetized shell and allows for the possibility that the planet could have "frozen in" a magnetic field. Aharonson et al. (2004) recognized that the expected remanent signature would have a dipolar component, as observed for Mercury. While the analysis of Aharonson et al. does not prove that Mercury's magnetic field is a consequence of remanence, it removes previous objections to the idea and broadens the currently allowable thermophysical range of the current core state. Stanley et al. (2005) discussed how MESSENGER could resolve the internal vs. crustal origin of the field. The power spectrum of the field measured by MESSENGER will provide insight into its origin, as would the detection of any temporal variability, which would point to an internally generated dynamo. If the field structure correlates with gravity indicating topography at the CMB, then a thermoelectric dynamo (Stevenson 1987) would be favored (Giampieri and Balogh 2002). Finally, small-scale magnetic structure with a shallow source depth would point to a crustal remanent field.

The question of the timescales of magnetic reversal versus crustal cooling remains to be addressed in future testing of this hypothesis. Reversal timescales can in principle be estimated from numerical dynamo models (e.g., Glatzmaier and Roberts 1995), and these can be compared to models of crustal cooling (Turcotte and Schubert 1982).

5.3 Core Dynamo Models

An active dynamo source for Mercury's field has been viewed as problematic because of discrepancies between the observed field's magnitude and theoretical estimates of the magnetic field strength produced by an Earth-like dynamo. Specifically, an Earth-like dynamo, driven by thermo-compositional core convection, would be expected to produce a much stronger field than observed at Mercury (Stevenson 1987; Schubert et al. 1988).

There are two independent methods for estimating the magnetic field strength generated by a dynamo. The first method, energy balance, involves balancing the gravitational energy release driving the dynamo and the ohmic energy dissipated through electrical currents. Using thermal evolution models for Mercury to estimate the gravitational energy, magnetic field strengths of the order of 10^5-10^7 nT are obtained (Stevenson et al. 1983; Stevenson 1987).

The second method, magnetostrophic balance, relies on assuming that Mercury's dynamo operates in the strong-field regime where the Lorentz force balances the Coriolis force. This balance results in an estimate for the magnetic field of $B = (2\dot{\psi}\rho \mathrm{Re}_M/\sigma)^{1/2}$, where B is the magnetic field, $\dot{\psi}$ is the planetary rotation rate, ρ is density, σ is electrical conductivity, $\mathrm{Re}_M = UL/\eta$ is the magnetic Reynolds number, η is the magnetic diffusivity, U is a typical velocity scale, and L is a typical length scale. For a magnetic Reynolds number Re_M on the order of 10–1,000 (10 is the minimum Re_M value for dynamo action), the estimated field strength is in the same range as obtained using energetic arguments.

The magnetic field estimates provided by these two methods do not immediately conflict with the observed field value since the estimate is of the field strength in the fluid core, rather than at some distance outside the core where the observations are made. Because the magnetic field is solenoidal, the core field can be represented in spherical harmonics using the toroidal-poloidal decomposition

$$B = B_T + B_P = \nabla \times T\hat{r} + \nabla \times \left(\nabla \times P\hat{r}\right), \tag{9}$$

where B_T and B_P are the toroidal and poloidal field components, respectively, T and P are the toroidal and poloidal scalars, respectively, and $\hat{r}$ is a unit vector in the radial direction. Because the toroidal field has no radial component, it is not observable outside the conducting core and only the poloidal field is measured outside the dynamo generation region. The magnetic field estimate given by the energy and magnetostrophic balance arguments pertains to the dominant magnetic field component in the core. Since the poloidal field at the core mantle boundary inferred from the measured magnetic dipole intensity cannot match the magnetic field estimates, it is most likely that the toroidal field is dominant in the core (unless the poloidal field inside the core is significantly larger than both the toroidal field in the core and the poloidal field at the core–mantle boundary).

A problem arises when one compares the dipole field strength at Mercury's core–mantle boundary, which is assumed to be representative of the poloidal field strength at the CMB, to the toroidal field strength in Mercury's core, estimated using the energy or magnetostrophic balance arguments. The ratio of these fields is $B_{\mathrm{dip}}/B_T \sim 10^{-2}-10^{-4}$. From a similar analysis of Earth's dynamo, $B_{\mathrm{dip}}/B_T \sim 10^{-1}$. These dynamo solutions for Mercury are problematic, because it appears that Mercury's dynamo produces a much smaller B_{dip}/B_T ratio than Earth's dynamo and it is unclear why this should be the case.

Additional testing of the viability of Mercury's magnetic field as a consequence of a core dynamo requires consideration of observed and expected field properties for the end-member thin-shell and thick-shell core geometries (see Fig. 8), where shell size reflects the thickness of the liquid iron region relative to the total core radius.

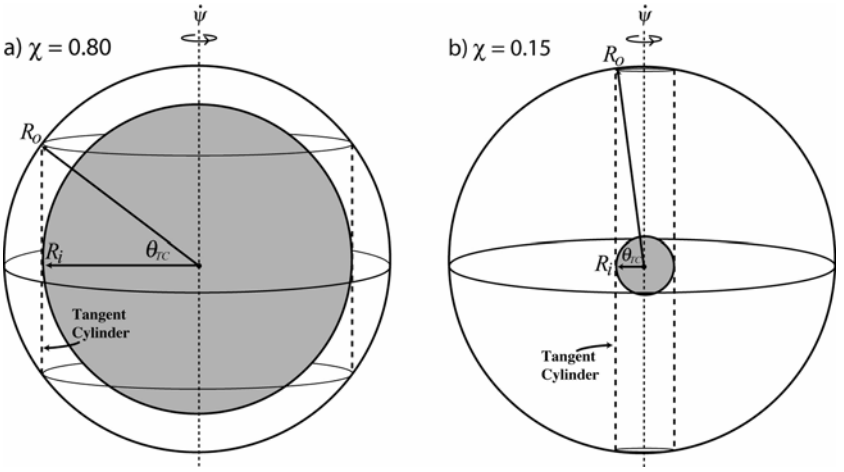

Fig. 8 Schematics of **(a)** thin-shell and **(b)** thick-shell dynamo models. Here R_i is the radius of the solid inner core, R_o is the radius of the liquid outer core, $\chi = R_i/R_o$, and θ_{TC} defines the angular size of the tangent cylinder

5.3.1 Thin-Shell Dynamo Models

One possible explanation for the difference in field partitioning is that Mercury's dynamo operates in a different core geometry than does Earth's. Thermal evolution models for Mercury (Stevenson et al. 1983; Stevenson 1987; Schubert et al. 1988) suggest that its core might consist of a thin fluid shell surrounding a large solid inner core. This thin-shell dynamo geometry is different from the thick-shell geometry of Earth's core ($R_i/R_o \approx 0.35$), a distinction that may lead to differences in the magnetic fields they produce.

A recent study (Stanley et al. 2005) of magnetic field partitioning and characteristics for various outer core shell thicknesses and Rayleigh numbers using a numerical dynamo model (Kuang and Bloxham 1997, 1999) demonstrated that some thin-shell dynamos can produce average $B_{\rm dip}/B_T$ ratios of $\sim 10^{-2}$. These ratios are variable in time and can be as low as $\sim 10^{-3}$, consistent with the theoretical values for Mercury. In these dynamos, both the ratio of poloidal field to toroidal field in the core (B_P/B_T) and the ratio of dipole field at the CMB to poloidal field in the core ($B_{\rm dip}/B_P$) are smaller than the Earth-like case.

In these thin-shell dynamo models, illustrated in Fig. 9, a strong, stable toroidal field is maintained inside the tangent cylinder through differential rotation. Little convection occurs in this region, and hence little poloidal field is produced from the strong toroidal field inside the tangent cylinder. Outside the tangent cylinder, only a few convection columns are present that can produce poloidal magnetic field from toroidal field. However, the toroidal field is much weaker in this region and very time dependent. The combination of a few convection cells and a weak toroidal field results in a much weaker and smaller-scale poloidal field produced in this region.

These Mercury-like dynamos occur over limited ranges of shell thickness and Rayleigh number. Such dynamos require both a thin-shell geometry in order to restrict the convection columns to the small region outside the tangent cylinder, so that they are not effective at interacting with toroidal field, as well as a relatively low Rayleigh number (close to the critical value for the onset of strong field dynamo action), so that convection is not yet generated inside the tangent cylinder. In intermediate shell geometries, the region inside the

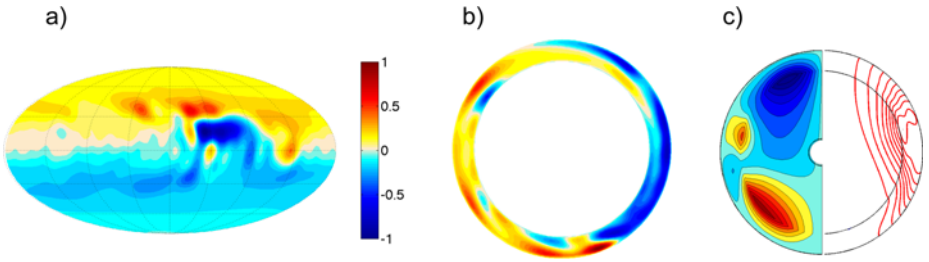

Fig. 9 Snapshot from the $R_i/R_o = 0.8$ case of Stanley et al. (2005). **(a)** Contours of the magnetic field on the CMB. **(b)** Contours of axial vorticity in the equatorial plane viewed from above. **(c)** Meridional slices showing (*left*) contours of the axisymmetric toroidal magnetic field and (*right*) the axisymmetric poloidal magnetic field lines. Because the poloidal field is far weaker than the toroidal field, the two vector fields are contoured independently in this figure. The *colorbar* in **(a)** applies to **(b)** and the left half of **(c)** as well

tangent cylinder is smaller and convection columns outside the tangent cylinder can interact with the majority of the toroidal field. At larger Rayleigh numbers, convection inside the tangent cylinder is effective at producing a strong poloidal field there, and hence Earth-like partitioning results.

5.3.2 Thick-Shell Dynamo Models

Recent thermal evolution modeling for Mercury has shown that the present ratio of the solid inner core radius to its outer core radius (R_i/R_o) is a sensitive function of core sulfur content and initial core temperature (Harder and Schubert 2001; Hauck et al. 2004). These results suggest that thick-shell dynamo models may be relevant to Mercury. Numerical simulations have been carried out to determine how dynamo action varies for a wide range of core geometries (Heimpel et al. 2005), covering $R_i/R_o = 0.15$ to 0.65. In these simulations, illustrated in Fig. 10, weak external magnetic fields, comparable to that observed for Mercury, are produced in strong-field, thick-shell cases with $R_i/R_o = 0.10{-}0.20$. The ratio of B_P/B_T is $\sim 10^{-2}$ in the case with $R_i/R_o = 0.15$. In contrast, cases with intermediate core geometries between $R_i/R_o = 0.25$ and 0.65 generate strong external dipole fields that are more Earth-like than the thick-shell cases.

For thick-shell dynamos (with $R_i/R_o < 0.25$), a single turbulent convection column is the preferred mode of convection. This single columnar structure dominates the poloidal flow in this simulation. Helical flow within the column acts locally to generate a poloidal magnetic field. A strong retrograde zonal flow also exists throughout the region outside the tangent cylinder. This strong zonal flow shears out the poloidal field into a toroidal magnetic field. Because poloidal field generation occurs only in a single, localized region, the total poloidal field energy is small. In contrast, the large-scale zonal shearing efficiently induces a strong large-scale toroidal magnetic field.

It should be noted that a similar mechanism operates in both the thin-shell $R_i/R_o = 0.80$ model of Fig. 9 (Stanley et al. 2005) and the thick-shell $R_i/R_o = 0.15$ model of Fig. 10 (Heimpel et al. 2005). Columnar convection generates the poloidal magnetic field in a relatively small portion of the core fluid, whereas toroidal magnetic field is induced by large-scale zonal flows that occur over a much larger fractional volume of the core. Thus, in both cases, the poloidal magnetic field is much weaker than the toroidal field because poloidal magnetic field generation is generated efficiently only in a small, localized region.

Magnetic field observations by MESSENGER should be able to distinguish between thick- and thin-shell dynamo scenarios. In both cases, localized strong radial magnetic

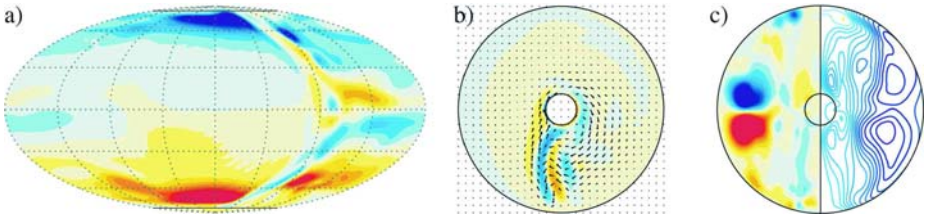

Fig. 10 Snapshot from the $R_i/R_o = 0.15$ case of Heimpel et al. (2005). **(a)** Contours of the magnetic field on the CMB. **(b)** Contours of axial vorticity in the equatorial plane, viewed from above. *Arrows* denote equatorial velocity vectors. The region of intense vorticity marks out the single turbulent convection column that develops in this model. The large-scale spiraling structure away from the convective region marks out the region of zonal shear. **(c)** Meridional slices showing (*left*) contours of the axisymmetric toroidal magnetic field and (*right*) the poloidal magnetic field lines. Because the poloidal field is far weaker than the toroidal field, the two vector fields are contoured independently in this figure

flux patches are produced outside the tangent cylinder where the convection cells generate poloidal field from toroidal field. Since the size of the tangent cylinder depends on the inner core size, the thin- and thick-shell core geometries have different tangent cylinders. The intersection of the tangent cylinder with the core–mantle boundary in a thick-shell geometry occurs at much higher latitudes ($\sim 81^\circ$ in the Heimpel et al. models) than in the thin-shell case ($\sim 37^\circ$ in the Stanley et al. models). If MESSENGER can determine the approximate latitude of these magnetic flux patches, it will be possible to determine the size of the tangent cylinder and hence whether the dynamo operates in a thick- or thin-shell geometry. Another difference between the thick- and thin-shell numerical models that may be of help in determining Mercury's core geometry is the tilt of the dipole component. The Stanley et al. thin-shell models have dipole tilts that vary significantly in time and can be quite large. In contrast, the Heimpel et al. models have a small dipole tilt that varies little in time. Finally, the tangent cylinder is the site of a shear boundary layer in many models of core flow. Such a large-scale shear can produce latitudinal gradients in secular variation that may be inverted to estimate the geometry of Mercury's core (e.g., Olson and Aurnou 1999; Pais and Hulot 2000).

6 Thermal Evolution Models

6.1 Mantle Structure and Dynamics

The possibility that Mercury's magnetic field is a consequence of a core dynamo would require that the planet's metallic core is at present at least partially molten. For thermal evolution models in which core–mantle differentiation occurred early and the core is either pure iron or an iron-nickel solid solution, an initially molten core should have frozen out by now (Siegfried and Solomon 1974; Cassen et al. 1976; Fricker et al. 1976).

Current understanding of Mercury's internal evolution has been developed in large part through simulation of long-term heat transfer through the planet's mantle. These models incorporate either, or both, conductive and convective mechanisms for heat loss during Mercury's history. Since the Mariner 10 flybys, modeling has provided insights into: (1) the planet's interior evolution within the constraint of (limited) global contraction as inferred from lobate scarps observed in images and interpreted as contractional in origin (Strom et al. 1975), and (2) the existence of an intrinsic magnetic field (Ness et al. 1975). Early models were based on the assumption that Mercury's mantle lost heat exclusively by conduction

and were important in establishing the significance of an alloying element in Mercury's large core to forestall complete core solidification and the accompanying ∼17 km of planetary contraction that would result [∼15 times more than that inferred from the lobate scarps (e.g., Solomon 1976)]. Furthermore, the necessity of a partially molten core in order to satisfy contraction estimates was also consistent with the requirement for a core dynamo origin for the magnetic field (i.e., an electrically conductive fluid shell).

Widespread recognition that terrestrial planetary mantles could be unstable to convection (Schubert et al. 1979) led to further work on Mercury's thermal evolution (Stevenson et al. 1983; Schubert et al. 1988). As would be expected, models that included the more efficient planetary cooling provided by mantle convection confirmed that a modest amount, at least 2–3 weight%, of an alloying element such as sulfur is necessary to limit contraction. However, it has also been demonstrated that even the enhanced cooling of mantle convection might not be sufficient to drive the core convection necessary for a modern dynamo (Schubert et al. 1988).

6.2 Parameterized Mantle Convection

A recent reanalysis of the thermal evolution of Mercury (Hauck et al. 2004) extended the parameterized mantle convection technique used in earlier studies to include the energetics of mantle partial melting and temperature- and pressure-dependent flow laws for mantle materials. This class of model is also able to account for the conductive transport of heat in the mantle when the thermal Rayleigh number is subcritical for convection. Such a transition from early convective to later conductive heat transport is directly applicable to Mercury's thin mantle, a transition that tends to stabilize it against convection relative to the other terrestrial planets. The time of such a convection-to-conduction transition depends on the details of mantle material properties such as rheology and the concentration of heat-producing elements, though a principal result is that the relatively low efficiency of cooling via conduction is an important element of models capable of satisfying the small amount of contractional strain recorded in lobate scarps (Hauck et al. 2004). As illustrated in Fig. 11, that study also demonstrated that models that strictly satisfied the dual requirements of ∼1−2 km of radial contraction since 4 Ga and a modern fluid outer core had >6.5 weight% sulfur content in the core, a creep-resistant (i.e., anhydrous) flow law for mantle material, and heat production provided primarily by the very long-lived isotope ^{232}Th. Figure 12 shows the timing of the transition from mantle convection to conduction as a function of bulk core sulfur content. At low sulfur contents most of the models have an inner core when the model starts; the size of the initial inner core decreases as sulfur content increases. Increasing sulfur content toward the peak at ∼7 weight % sulfur results in a greater volume of inner core crystallizing over the age of the solar system. Past the peak, the effect of the adopted initial temperature profiles and core states is not apparent. The behavioral transition at ∼7 weight % sulfur is probably controlled by the volume of core crystallized and underscores the need to couple core and mantle evolution in modeling.

The dominance of ^{232}Th in heat production in these models is predicted for the silicate vaporization scenario for Mercury's anomalously high iron-silicate ratio (Fegley and Cameron 1987). However, if the radial contraction is underestimated by even a factor of two, including unrecognized mechanisms such as low-amplitude, long-wavelength folding that might accommodate strain in addition to that localized and recorded in the lobate scarps, then the concentration of heat-producing elements is unconstrained, though the bulk sulfur content of the core would likely need to be greater than about 6 weight% to prevent greater contraction (Hauck et al. 2004). Thermal convection in the outer core, a prerequisite for some dynamo

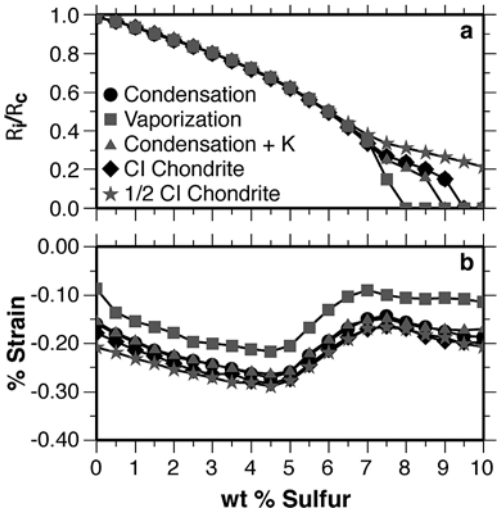

Fig. 11 Comparison of the effects of heat-producing element concentrations on **(a)** normalized inner core radius, and **(b)** surface strain as functions of bulk core sulfur content for a dry-olivine mantle rheology, mantle melt extraction and crustal growth, and an initial upper mantle temperature of 1,800 K. From Hauck et al. (2004)

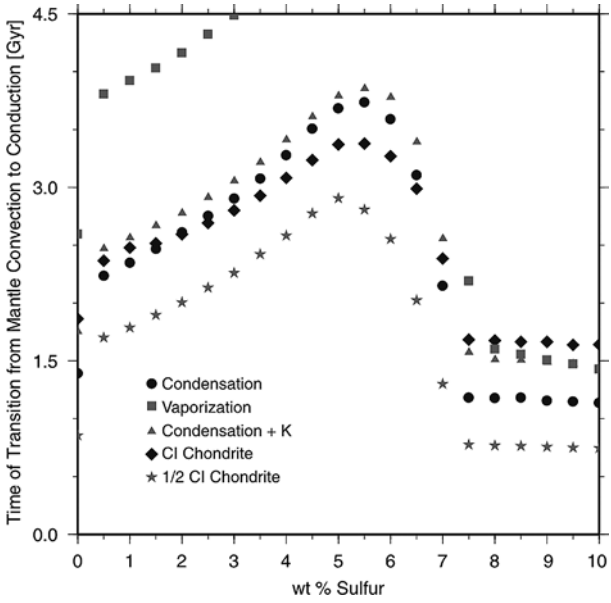

Fig. 12 Time of transition from mantle convection to conduction in Gy, where 4.5 Gy corresponds to the present, for several models of interior heat production

models, is possible only under limited conditions: a weak (e.g., wet) mantle flow law, large sulfur content of the core, and global contraction a factor of two or more greater than current estimates. The likelihood and importance of heat production from ^{40}K in the core (Murthy et al. 2003) have not been thoroughly assessed for Mercury. Compositionally induced convection, fueled by the sinking of solid iron-nickel in a cooling outer core in which light-element (e.g., sulfur) enrichment progressively increases, eases these restrictions considerably and may be favored if Mercury's magnetic field has a dynamo origin.

7 Looking Ahead

Constraints on obliquity and libration provided by Earth-based radar (Margot et al. 2007) prior to MESSENGER will allow improved a priori estimates of these parameters, permitting more accurate measurements to be recovered by MESSENGER. These, combined with improved estimates of the degree-two gravitational harmonic coefficients from radio tracking of the MESSENGER spacecraft (Srinivasan et al. 2007), along with refined geochemical models enabled by MESSENGER observations of surface chemistry (Boynton et al. 2007), will permit a direct estimate of Mercury's core size. Any difference (or not) in the forced libration of Mercury's surface and deep interior as determined by tracking the libration in the long-wavelength topography and gravity fields, respectively, will allow the viscous coupling of the lithosphere and deep interior to be estimated (Zuber and Smith 1997). An improved knowledge of the present core state will allow reconstructions of the planet's thermal evolution over time to be sharpened.

Recent observational evidence that Mercury has a liquid outer core (Margot et al. 2007) strengthens the hypothesis that the planet's magnetic field is generated by a dynamo, though it does not invalidate the possibility that a remanent crustal field could potentially contribute to the field observed by Mariner 10 (Stephenson 1976; Aharonson et al. 2004). The current state of dynamo modeling demonstrates that a dynamo solution for Mercury's magnetic field is possible on the grounds that both thin-shell and thick-shell dynamos can produce fields with Mercury-like partitioning of toroidal and poloidal fields. However, the success of these models does not rule out crustal magnetization or a thermoelectric dynamo (see Stevenson 1987) as the source of Mercury's field. Future measurements of Mercury's magnetic field by the MESSENGER mission should resolve the issue. If any field variability in time is observed, then an active dynamo source will be indicated. If the field structure is correlated with gravity signatures at wavelengths appropriate to topography at the core–mantle boundary, then a thermoelectric dynamo will be the most likely answer (Giampieri and Balogh 2002). Any small-scale structure with shallow source depths is crustal in origin. If no time variation is detected, such a result would not rule out a dynamo source; rather it would mean that the timescale of secular variation is longer than the length of time the observations have been carried out. Determining whether the field is crustal or dynamo generated in this case may be possible if evidence of an effect due to the tangent cylinder is seen. If the character of the magnetic field is different inside and outside the tangent cylinder due to different convection patterns in these regions, then a dynamo source for the field may be indicated.

The Mercury Planetary Orbiter spacecraft in the BepiColombo mission, expected to explore Mercury subsequent to MESSENGER, is planned to be in a comparatively low-eccentricity orbit with an equatorial periapsis (Grard and Balogh 2001). If implemented as currently planned, BepiColombo will provide much-improved altimetric and gravitational coverage of the southern hemisphere of Mercury, allowing global models of crustal and lithosphere structure and refinement of rotational state. Measurements of Mercury's magnetic field, coupled with those made by MESSENGER, will extend the temporal baseline over which temporal variations in the internal field may be discernable. These observations will collectively allow a fuller assessment of the relationship between Mercury's core state and the planet's thermal and geologic evolution.

Acknowledgements The MESSENGER mission is supported by NASA's Discovery Program through contract NASW-00002 with the Carnegie Institution of Washington.

References

M.H. Acuña et al., Science **279**, 1676–1680 (1998)
M.H. Acuña et al., Science **284**, 790–793 (1999)
M.H. Acuña et al., J. Geophys. Res. **106**, 23,403–23,417 (2001)
J.B. Adams et al., in *Basaltic Volcanism on the Terrestrial Planets*, ed. by T.R. McGetchin, R.O. Pepin, R.J. Phillips (Pergamon, New York, 1981), pp. 439–490
O. Aharonson, M.T. Zuber, S.C. Solomon, Earth Planet. Sci. Lett. **218**, 261–268 (2004)
J.D. Anderson, G. Colombo, P.B. Esposito, E.L. Lau, G.B. Trager, Icarus **71**, 337–349 (1987)
J.D. Anderson, R.F. Jurgens, E.L. Lau, M.A. Slade, III, G. Schubert, Icarus **124**, 690–697 (1996)
B.G. Bills, G.A. Neumann, D.E. Smith, M.T. Zuber, J. Geophys. Res. **110**, E07004 (2005). doi:10.1029/2004JE002376
M.B. Boslough, E.P. Chael, T.G. Trucano, D.A. Crawford, D.L. Campbell, in *The Cretaceous-Tertiary Event and Other Catastrophes in Earth History, Spec. Paper 307*, ed. by G. Ryder, D. Fastovsky, S. Gartner (Geol. Soc. Am., Boulder, 1996), pp. 541–550
W.V. Boynton et al., Space Sci. Rev. (2007, this issue). doi:10.1007/s11214-007-9258-3
B.A. Buffett, J. Geophys. Res. **97**, 19,581–19,597 (1992)
B.A. Buffett, E.J. Garnero, R. Jeanloz, Science **290**, 1338–1342 (2000)
K.C. Burke et al., in *Basaltic Volcanism on the Terrestrial Planets*, ed. by T.R. McGetchin, R.O. Pepin, R.J. Phillips (Pergamon, New York, 1981), pp. 803–898
J.B. Burns, Icarus **28**, 453–458 (1976)
A.G.W. Cameron, Icarus **64**, 285–294 (1985)
P. Cassen, R.E. Young, G. Schubert, R.T. Reynolds, Icarus **28**, 501–508 (1976)
J.F. Cavanaugh et al., Space Sci. Rev. (2007, this issue). doi:10.1007/s11214-007-9273-4
M.J. Cintala, C.A. Wood, J.W. Head, *Proc. Lunar Planet. Sci. Conf. 8th*, 1977, pp. 3409–3425
G. Colombo, Nature **208**, 575 (1965)
G. Colombo, I.I. Shapiro, Astrophys. J. **145**, 296–307 (1966)
J.E.P. Connerney, N.F. Ness, in *Mercury*, ed. by F. Vilas, C.R. Chapman, M.S. Matthews (Univ. Ariz. Press, Tucson, 1988), pp. 494–513
A.C.M. Correia, J. Laskar, Nature **429**, 848–850 (2004)
C.C. Counselman, Ph.D. thesis, Mass. Inst. Tech., Cambridge, 1969
C.C. Counselman, I.I. Shapiro, *Symposia Mathematica, Instituto Nazionale di Alta Matematica*, vol. III (Academic, London, 1970) pp. 121–169
G.A. de Wijs et al., Nature **392**, 805–807 (1998)
D. Dzurisin, J. Geophys. Res. **83**, 383–386 (1978)
A. Einstein, Annalen der Physik, 1916, 46 pp
B.J. Fegley, A.G.W. Cameron, Earth Planet. Sci. Lett. **82**, 207–222 (1987)
L. Fleitout, P.G. Thomas, Earth Planet. Sci. Lett. **58**, 104–115 (1982)
P.E. Fricker, R.T. Reynolds, A.L. Summers, P.M. Cassen, Nature **259**, 293–294 (1976)
G. Giampieri, A. Balogh, Planet. Space Sci. **50**, 757–762 (2002)
G.A. Glatzmaier, P.H. Roberts, Nature **377**, 203–209 (1995)
P. Goldreich, S.J. Peale, Astron. J. **71**, 425–438 (1966)
P. Goldreich, A. Toomre, J. Geophys. Res. **74**, 2555–2567 (1969)
R. Grard, A. Balogh, Planet. Space Sci. **49**, 1395–1407 (2001)
H.P. Greenspan, G.N. Howard, J. Fluid Mech. **17**, 17,385–17,404 (1963)
B. Hapke, G.E.J. Danielson, K. Klaasen, L. Wilson, J. Geophys. Res. **80**, 2431–2443 (1975)
H. Harder, G. Schubert, Icarus **151**, 118–122 (2001)
J.K. Harmon, D.B. Campbell, in *Mercury*, ed. by F. Vilas, C.R. Chapman, M.S. Matthews (Univ. Ariz. Press, Tucson, 1988), pp. 101–117
J.K. Harmon, D.B. Campbell, D.L. Bindschadler, J.W. Head, I.I. Shapiro, J. Geophys. Res. **91**, 385–401 (1986)
S.A. Hauck II, A.J. Dombard, R.J. Phillips, S.C. Solomon, Earth Planet. Sci. Lett. **22**, 713–728 (2004)
J.W. Head et al., in *Basaltic Volcanism on the Terrestrial Planets*, ed. by T.R. McGetchin, R.O. Pepin, R.J. Phillips (Pergamon, New York, 1981), pp. 701–800
J.W. Head et al., Space Sci. Rev. (2007, this issue). doi:10.1007/s11214-007-9263-6
M.H. Heimpel, J.M. Aurnou, F.M. Al-Shamali, N. Gomez Perez, Earth Planet. Sci. Lett. **236**, 542–557 (2005)
F. Herbert, M. Wiskerchen, C.P. Sonett, J.K. Chao, Icarus **28**, 489–500 (1976)
R. Hide, Phil. Trans. R. Soc. Lond. **A328**, 351–363 (1989)
L.V. Holin, Radiophys. Quantum Electron. **31**, 371–374 (1988)
L.V. Holin, Radiophys. Quantum Electron. **35**, 284–287 (1992)
L.V. Holin, Meteorit. Planet. Sci. **38**(Suppl.), A9 (2003)

H.G. Hughes, F.N. App, T.R. McGetchin, Phys. Earth Planet. Interiors **15**, 251–263 (1977)
R. Jeanloz, D.L. Mitchell, A.L. Sprague, I. de Pater, Science **268**, 1455–1457 (1995)
W.M. Kaula, *Theory of Satellite Geodesy: Applications of Satellites to Geodesy* (Blaisdell, Waltham, 1966), 124 pp
W.M. Kaula, *An Introduction to Planetary Physics: The Terrestrial Planets* (Wiley, New York, 1968), 490 pp
W.M. Kaula, J. Geophys. Res. **84**, 999–1008 (1979)
G. Kletetschka, P.J. Wasilewski, P.T. Taylor, Earth Planet. Sci. Lett. **176**, 469–479 (2000a)
G. Kletetschka, P.J. Wasilewski, P.T. Taylor, Meteorit. Planet. Sci. **35**, 895–899 (2000b)
W. Kuang, J. Bloxham, Nature **389**, 371–374 (1997)
W. Kuang, J. Bloxham, J. Comp. Phys. **153**, 51–81 (1999)
K. Lambeck, S. Pullan, Phys. Earth Planet. Interiors **22**, 29–35 (1980)
M.A. Leake, in *Advances in Planetary Geology*. NASA TM-84894, Washington, DC, 1982, pp. 3–535
J.S. Lewis, Earth Planet. Sci. Lett. **15**, 286–290 (1972)
J.S. Lewis, Ann. Rev. Phys. Chem. **24**, 339–351 (1973)
M.C. Malin, *Proc. Lunar Planet. Sci. Conf. 9th*, 1978, pp. 3395–3409
J.-L. Margot, S.J. Peale, R.F. Jurgens, M.A. Slade, I.V. Holin, Science **316**, 710–714 (2007)
T.A. Maxwell, A.W. Gifford, *Proc. Lunar Planet. Sci. Conf. 11th*, 1980, pp. 2447–2462
T.B. McCord, R.N. Clark, J. Geophys. Res. **84**, 7664–7668 (1979)
W.B. McKinnon, ed. by in R.B. Merrill, P.H. Schultz, Multi-ring basins, proc. Lunar Planet. Sci. **12**, Part A, 1981, Pergamon Press, New York, pp. 259–273
W.B. McKinnon, H.J. Melosh, Icarus **44**, 454–471 (1980)
H.J. Melosh, Icarus **31**, 221–243 (1977)
H.J. Melosh, *Proc. Lunar Planet. Sci. Conf. 9th*, 1978, pp. 3513–3525
H.J. Melosh, D. Dzurisin, Icarus **35**, 227–236 (1978)
H.J. Melosh, W.B. McKinnon, Geophys. Res. Lett. **5**, 985–988 (1978)
H.J. Melosh, W.B. McKinnon, in *Mercury*, ed. by F. Vilas, C.R. Chapman, M.S. Matthews (Univ. Ariz. Press, Tucson, 1988), pp. 374–400
W.H. Munk, G.J.F. MacDonald, *The Rotation of the Earth* (Cambridge Univ. Press, New York, 1960), 323 pp
B.C. Murray, J. Geophys. Res. **80**, 2342–2344 (1975)
B.C. Murray et al., Science **185**, 169–179 (1974)
V.R. Murthy, W. van Westrenen, Y. Fei, Nature **423**, 163–165 (2003)
N.F. Ness, Space Sci. Rev. **21**, 527–553 (1978)
N.F. Ness, Ann. Rev. Earth Planet. Sci. **7**, 249–288 (1979)
N.F. Ness, K.W. Behannon, R.P. Lepping, Y.C. Whang, K.H. Schatten, Science **185**, 151–160 (1974)
N.F. Ness, K.W. Behannon, R.P. Lepping, Y.C. Whang, J. Geophys. Res. **80**, 2708–2716 (1975)
N.F. Ness, K.W. Behannon, R.P. Lepping, Y.C. Whang, Icarus **28**, 479–488 (1976)
G.A. Neumann, M.T. Zuber, D.E. Smith, F.G. Lemoine, J. Geophys. Res. **101**, 16,841–16,863 (1996)
V.R. Oberbeck, W.L. Quaide, R.E. Arvidson, H.R. Aggarwal, J. Geophys. Res. **82**, 1681–1698 (1977)
P. Olson, J. Aurnou, Nature **402**, 170–173 (1999)
A. Pais, G. Hulot, Phys. Earth Planet. Interiors **118**, 291–316 (2000)
S.J. Peale, Astron. J. **74**, 483–489 (1969)
S.J. Peale, Astron. J. **79**, 722–744 (1974)
S.J. Peale, Nature **262**, 765–766 (1976)
S.J. Peale, Icarus **48**, 143–145 (1981)
S.J. Peale, in *Mercury*, ed. by F. Vilas, C.R. Chapman, M.S. Matthews (Univ. Ariz. Press, Tucson, 1988), pp. 461–493
S.J. Peale, Icarus **178**, 4–18 (2005)
S.J. Peale, Icarus **181**, 338–347 (2006)
S.J. Peale, A.P. Boss, J. Geophys. Res. **82**, 743–749 (1977)
S.J. Peale, R.J. Phillips, S.C. Solomon, D.E. Smith, M.T. Zuber, Meteorit. Planet. Sci. **37**, 1269–1283 (2002)
S.J. Peale, M. Yseboot, J.-L. Margot, Icarus **87**, 365–373 (2007)
G.H. Pettengill, R.B. Dyce, Nature **206**, 1240 (1965)
T.R. Quinn, S. Tremaine, M. Duncan, Astron. J. **101**, 2287–2305 (1991)
A.E. Ringwood, *The Origin of the Earth and Moon* (Springer, New York, 1979), 295 pp
M.S. Robinson, P.G. Lucey, Science **275**, 197–200 (1997)
P. Rochette, J.P. Lorand, G. Fillion, V. Sautter, Earth Planet. Sci. Lett. **190**, 1–12 (2001)
N.T. Roseveare, *Mercury's Perihelion from Le Verrier to Einstein* (Oxford Sci. Publications, Clarendon Press, 1982), 208 pp
S.K. Runcorn, Nature **253**, 701–703 (1975a)
S.K. Runcorn, Phys. Earth Planet. Interiors **10**, 327–335 (1975b)

C.T. Russell, D.N. Baker, J.A. Slavin, in *Mercury*, ed. by F. Vilas, C.R. Chapman, M.S. Matthews (Univ. Ariz. Press, Tucson, 1988), pp. 514–561
V.S. Safronov, Icarus **33**, 1–12 (1978)
G. Schubert, P.M. Cassen, R.E. Young, Icarus **38**, 192–211 (1979)
G. Schubert, M.N. Ross, D.J. Stevenson, T. Spohn, in *Mercury*, ed. by F. Vilas, C.R. Chapman, M.S. Matthews (Univ. Ariz. Press, Tucson, 1988), pp. 429–460.
P.H. Schultz, D.E. Gault, *Proc. Lunar Sci. Conf. 6th*, 1975a, pp. 2845–2862
P.H. Schultz, D.E. Gault, Moon **12**, 159–177 (1975b)
I.I. Shapiro, G.H. Pettengill, M.E. Ash, R.P. Ingalls, D.B. Campbell, R.B. Dyce, Phys. Rev. Lett. **28**, 1594–1597 (1972)
R.W. Siegfried, II, S.C. Solomon, Icarus **23**, 192–205 (1974)
M. Simons, S.C. Solomon, B.H. Hager, Geophys. J. Int. **131**, 24–44 (1997)
J.A. Slavin et al., Space Sci. Rev. (2007, this issue). doi:10.1007/s11214-007-9154-x
J.C. Smith, G.H. Born, Icarus **27**, 51–53 (1976)
S.C. Solomon, Icarus **28**, 509–521 (1976)
S.C. Solomon, Phys. Earth Planet. Interiors **15**, 135–145 (1977)
S.C. Solomon, Geophys. Res. Lett. **5**, 461–464 (1978)
S.C. Solomon, J.W. Head, Rev. Geophys. **18**, 107–141 (1980)
S.C. Solomon et al., in *Basaltic Volcanism on the Terrestrial Planets*, ed. by T.R. McGetchin, R.O. Pepin, R.J. Phillips (Pergamon, New York, 1981), pp. 1129–1233
S.C. Solomon et al., Planet. Space Sci. **49**, 1445–1465 (2001)
A.L. Sprague, R.W.H. Kozlowski, F.C. Witteborn, D.P. Cruikshank, D.H. Wooden, Icarus **109**, 156–167 (1994)
P.D. Spudis, J.E. Guest, in *Mercury*, ed. by F. Vilas, C.R. Chapman, M.S. Matthews (Univ. Ariz. Press, Tucson, 1988), pp. 118–164
P.D. Spudis, J.G. Prosser, Map I-1689, U.S. Geol. Survey, Denver, CO, 1984
D.K. Srinivasan, M.E. Perry, K.B. Fielhauer, D.E. Smith, M.T. Zuber, Space Sci. Rev. (2007, this issue). doi:10.1007/s11214-007-9270-7
L.J. Srnka, Phys. Earth Planet. Interiors **11**, 184–190 (1976)
E.M. Standish, Astron. Astrophys. **233**, 463–466 (1990)
E.M. Standish, X.X. Newhall, J.G. Williams, D.K. Yeomans, in *Explanatory Supplement to the Astronomical Almanac*, ed. by P.K. Seidelmann (Univ. Sci. Books, Mill Valley, 1992), pp. 279–323
S. Stanley, J. Bloxham, W.E. Hutchison, M.T. Zuber, Earth Planet. Sci. Lett. **234**, 27–38 (2005)
A. Stephenson, Earth Planet. Sci. Lett. **28**, 454–458 (1976)
D.J. Stevenson, Rept. Prog. Phys. **46**, 555–620 (1983)
D.J. Stevenson, Earth Planet. Sci. Lett. **82**, 114–120 (1987)
D.J. Stevenson, T. Spohn, G. Schubert, Icarus **54**, 466–489 (1983)
K. Stewartson, P.H. Roberts, J. Fluid Mech. **17**, 1–20 (1963)
R.G. Strom, Phys. Earth Planet. Interiors **15**, 156–172 (1977)
R.G. Strom, Space Sci. Rev. **24**, 3–70 (1979)
R.G. Strom, in *The Geology of the Terrestrial Planets*, ed. by M.H. Carr (NASA, Washington, 1984), pp. 13–55
R.G. Strom, N.J. Trask, J.E. Guest, J. Geophys. Res. **80**, 2478–2507 (1975)
A.M.K. Szeto, S. Xu, J. Geophys. Res. **102**, 27,651–27,657 (1997)
P.G. Thomas, P. Masson, L. Fleitout, in *Mercury*, ed. by F. Vilas, C.R. Chapman, M.S. Matthews (Univ. Ariz. Press, Tucson, 1988), pp. 401–428
A. Toomre, in *The Earth–Moon System*, ed. by B.G. Marsden, A.G.W. Cameron (Plenum, New York, 1966), pp. 33–45
N.J. Trask, J.E. Guest, J. Geophys. Res. **80**, 2462–2477 (1975)
N.J. Trask, R.G. Strom, Icarus **28**, 559–563 (1976)
D.L. Turcotte, G. Schubert, *Geodynamics: Applications of Continuum Physics to Geologic Problems* (Wiley, New York, 1982), 450 pp
H.C. Urey, Geochim. Cosmochim. Acta **1**, 209–277 (1951)
W.R. Ward, Astron. J. **80**, 64–69 (1975)
T.R. Watters, M.S. Robinson, A.C. Cook, Geology **26**, 991–994 (1998)
T.R. Watters, M.S. Robinson, C.R. Bina, P.D. Spudis, Geophys. Res. Lett. **31**, L04701 (2004). doi:10.1029/2003GL019171
S.J. Weidenschilling, Icarus **35**, 99–111 (1978)
G.W. Wetherill, in *Mercury*, ed. by F. Vilas, C.R. Chapman, M.S. Matthews (Univ. Ariz. Press, Tucson, 1988), pp. 670–691
D.E. Wilhelms, Icarus **28**, 551–558 (1976)

J.G. Williams, D.H. Boggs, C.F. Yoder, J.T. Ratcliff, J.O. Dickey, J. Geophys. Res. **10**, 27,933–27,968 (2001)
J.A. Wood et al., in *Basaltic Volcanism on the Terrestial Planets*, ed. by T.R. McGetchin, R.O. Pepin, R.J. Phillips (Pergamon, New York, 1981), pp. 634–699
C.F. Yoder, in *Global Earth Physics, A Handbook of Physical Constants*, ed. by T.J. Ahrens (American Geophys. Un., Washington, 1995), pp. 1–31
C.F. Yoder, A.S. Konopliv, D.-N. Yuan, E.M. Standish, W.M. Folkner, Science **300**, 299–303 (2003)
M. Yseboodt, J.-L. Margot, Icarus **181**, 327–337 (2006)
M.T. Zuber, J. Geophys. Res. **92**, E541–E551 (1987)
M.T. Zuber, D.E. Smith, Lunar Planet Sci. **27**, 1637–1638 (1997)
M.T. Zuber, D.E. Smith, F.G. Lemoine, G.A. Neumann, Science **266**, 1839–1843 (1994)